Asymmetric supercapacitor based on VS$_2$ nanosheets and activated carbon materials

Tshifhiwa M. Masikhwa, Farshad Barzegar, Julien K. Dangbegnon, Abdulhakeem Bello, Moshawe J. Madito, Damilola Momodu and Ncholu Manyala[*]

Department of Physics, Institute of Applied Materials, SARCHI Chair in Carbon Technology and Materials, University of Pretoria, Pretoria 0028, South Africa.

* Corresponding author: Tel: +27 (0)12 420 3549; fax: +27 (0)12 420 2516. E-mail: ncholu.manyala@up.ac.za (N. Manyala).

ABSTRACT

VS$_2$ nanosheets as the positive electrode and the activated carbon (AC) as the negative electrode with a 6 M KOH solution as electrolyte were fabricated as an asymmetric supercapacitor. These materials were combined to maximize the specific capacitance and to enlarge the potential window, therefore improving the energy density of the device. A specific capacitance of 155 F g^{-1} at 1 A g^{-1} with a maximum energy density as high as 42 Wh kg^{-1} and a power density of 700 W kg^{-1} was obtained for the asymmetric supercapacitor within the voltage range of 0 – 1.4 V. The supercapacitor also exhibited a good stability with ~ 99% capacitance retention and no capacitance loss after 5000 cycles at a current density of 2 Ag^{-1}.

Keywords: VS$_2$, electrochemical properties, activated carbon, asymmetric device, supercapacitor, energy storage

Introduction

Recently, supercapacitors which are advanced electrochemical energy storage systems , have been a hot topic due to their numerous advantages in power source applications such as short-term power sources for mobile electronic devices and auxiliary power sources for hybrid electric vehicles (HEV) [1–3]. Supercapacitors also known as ultracapacitors or electrochemical capacitors are energy storage devices that exhibit high power density but a relatively low energy density as compared to rechargeable batteries. Thus, there has been a massive focus by researchers to improve on the supercapacitor technology in order to enhance the energy density to at least the level of the of rechargeable battery systems. Beside the high power density, supercapacitors also show excellent properties such as long cycle life, rapid energy deliverance and long stability as compared to rechargeable batteries. The performance of supercapacitors to a large extent depends on the nature of the electrode material [4,5].

Typically, supercapacitors are categorized into three types based on their charge-storage mechanism, namely, electrical double-layer capacitors (EDLCs), faradaic and hybrid capacitors [2]. The storage mechanism in EDLCs arises from the accumulation of charges at the electrode/electrolyte interface that results in a non-faradaic reaction, whereas faradaic storage mechanism results from the fast redox reaction (faradaic reaction) [6].

Hybrid capacitors are obtained from either making the composites of the two materials or/and as positive and negative electrodes to form asymmetric cell, respectively, with different charge storage mechanism. An example could be an EDLC-type material as negative electrode and a faradaic-type material as positive electrode. This offers the possibility of synergizing the advantages of both electrodes such as the high electrical conductivity and stability of EDLC materials and the high specific capacitance of faradic or pseudo-capacitance materials. The properties of the resulting hybrid device lies between a supercapacitor and a battery [7]. Asymmetric supercapacitors are a special type of hybrid

capacitors obtained by mounting an EDLC carbon material electrode with a faradaic-type material electrode in order to increase the energy density by utilizing the resulting wide operating voltage window. This should not be detrimental to the cyclic stability attributed to carbon-based materials as well as the excellent power density from the higher capacitance of the faradaic-type material [7–10].

The carbon-based nanomaterials such as activated carbon (AC), carbon nanotubes (CNTs), graphene [11–15] are frequently used as the negative electrodes of asymmetric supercapacitors due to their stability in the negative potential region, good electronic conductivity, large surface area and relatively low-cost.[16–18] Activated carbon (AC) is the most suitable negative electrode material adopted for hybrid capacitors due to the numerous merits listed above but also due to its facile preparation process [19,20].

Various transition metal oxides and conductive polymers [21–25] are mostly used as positive electrodes due to their fast and reversible electron exchange reactions at the electrode interface which contribute to the high power densities and high capacitance of asymmetric supercapacitors. [26–34].

In recent years, metal chalcogenides materials have been considered for electrochemical energy storage applications due to their diverse chemical and physical properties [35]. For example, two-dimensional (2D) layered transition-metal dichalcogenides (TMDs) such as MoS_2, CoS_2, VS_2 and NiS_2 have been extensively studied for applications in electrochemical supercapacitors due to their promising electrochemical performance [36–38]. Numerous studies involving vanadium sulfides have been reported for various applications [37,39–42]. Pandurangan *et al* reported the synthesis of VS_2/rGO nanosheets by an rGO-assisted phase transformation via annealing of VS_4/rGO sheets at 350 °C for electro-catalysts of hydrogen evolution reaction[43]. Similarly, Satyajit *et al* also provided a detailed study of VS_4/rGO, sheets synthesized by a facile one-step hydrothermal route and an enhanced supercapacitor

performance of the VS_4/RGO[39]. The experimental results were further confirmed by computational simulations to further provide useful insights into the design of efficient energy storage devices. However, there have been little or no reports on the fabrication of an asymmetric capacitor with activated carbon from polymer based materials as the anode and VS_2 as the cathode in an aqueous electrolyte.

In this work, we report on the design of an asymmetric capacitor based on 3D interconnected activated carbon as negative electrode and mesoporous VS_2 nanosheets as positive electrode material. The hybrid material indicated high rate capability compared with a pure VS_2 nanosheets electrode. The VS_2//AC asymmetric supercapacitor could perform reversibly at a high cell voltage of 1.4 V in 6M KOH .The VS_2//AC asymmetric exhibited a specific capacitance of 155 F g^{-1} at 1 A g^{-1} with a maximum energy density as high as 42 Wh kg^{-1} and a power density of 700 W kg^{-1}. Furthermore, the supercapacitor also exhibited a good stability with ~ 99% capacitance retention and no capacitance loss after 5000 cycles at a current density of 2 Ag^{-1}.

Experimental

Materials

Ammonium vanadate ((NH_4VO_3), purity > 99.99%), thioacetamide ((CH_3CSNH_2 Sigma–Aldrich, ≥99%), Ammonia (NH_3, ≥ 99.95%) and polyvinyl alcohol (PVA, 99+ % hydrolyzed) were purchased from Sigma-Aldrich. Nickel foam was purchased from (Alantum, Munich, Germany), potassium hydroxide (KOH, min 85%) and urea (purity ≥ 98%) were purchased from Merck (South Africa).

Synthesis of VS₂ nanosheets

Scheme 1 shows the schematic method used to prepare the VS$_2$ nanosheets in this study. Ammonium metavanadate (NH$_4$VO$_3$) (2 mmol) was added to an 18 ml mixture of 15 ml deionized water and 3 ml ammonia, accompanied by vigorous stirring to completely dissolve the ammonium vanadate. Subsequently, thioacetamide (CH$_3$CSNH$_2$) (10 mmol) was added to the above solution under vigorous stirring. The final homogeneous solution was transferred into a sealed Teflon-lined stainless-steel autoclave and kept at a temperature of 180° C for 20 h. After cooling to room temperature, the black powder was washed with deionized water and dried at 60 $^\circ$C. The formation of the nanosheets morphology of VS$_2$ electrode includes two steps: An initial nucleating stage and a crystal growth stage including an Ostwald ripening process, which is known for the development of nanosheets metal sulfide structures [44]. In the early stage, various functional groups present in the reaction vessel, such as –NH$_2$, –COOH, and –SH, react with V^{4+} ions to form V-S complexes, which then decay to form VS$_2$ nuclei in the latest stage of the synthesis mechanism [45]. In the second stage, the nanosheets structures form as a result of the Ostwald ripening and self-assembly of the VS$_2$ sheets. Throughout the reaction, the hydrolysis of thioacetamide produces HS$^-$, which decreases V^{5+} to V^{4+} and layered VS$_2$ structures are formed[46].

Scheme 1: Preparation procedure of VS$_2$ nanosheets.

Synthesis of Activated carbon

Activated carbon used for the production of the composite materials was prepared as reported in our earlier work [47,48]. Briefly, graphene foam (GF) and polyvinyl alcohol (PVA) were used as starting material for the production of a hydrogel, which was then used to produce porous carbon materials after the activation process. The activated material was neutralized with 0.1 M HCl, washed with deionised water and dried at 120 °C for 12 h after which samples were characterized.

Structure and morphology characterization

The morphology of the prepared VS_2 and activated carbon electrodes was studied using the high-resolution Zeiss Ultra plus 55 field emission scanning electron microscope (FE-SEM) operated at 2.0 kV. Energy dispersive x-ray (EDX) patterns were taken with a JEOL 5800LV microscope equipped with an energy-dispersive X-ray spectrometer operated at 20 kV and was used to estimate the elemental composition of the produced materials. Transmission electron microscopy (TEM) micro-images and selected area electron diffraction (SAED) observations were carried out with a JEOL JEM-2100F microscope operated at 200 kV (Akishima-shi, Japan). X-ray diffraction (XRD) patterns of the prepared materials were collected using an XPERT-PRO diffractometer (PANalytical BV, Netherlands) with theta/2theta geometry, operating with a cobalt tube at 50 kV and 30 mA and reflection geometry at 2θ values ranging from 30–90° with a step size of 0.01°. The Raman spectra were recorded using a WITEC-Alpha 300R Plus confocal Raman spectrometer (WITEC GmbH, Ulm, Germany).with a 532-nm laser. X-ray photoelectron spectroscopy (XPS, K-alpha, Thermo Fisher) with monochromatic Al Kα radiation as the X-ray source was used to irradiate the sample surface and determine the chemistries of the samples synthesized in powder form. Nitrogen adsorption–desorption isotherms were measured at -196°C using a

Micromeritics ASAP 2020. All the samples were degassed at 180° C for more than 12 h under vacuum conditions. The surface area was calculated by the Brunauer–Emmett–Teller (BET) method from the adsorption branch in the relative pressure range (P/P_0) of 0.01–1.

Electrode preparation and electrochemical characterization.

All electrochemical measurements were carried out using a Biologic VMP-300 potentiostat (Knoxville TN 37,930, USA) controlled by the EC-Lab® V10.37 software. The three electrode measurements were performed for both AC and VS_2 serving as the working electrodes, Ag/AgCl (3 MKCl) serving as the reference electrode and glassy carbon plate as the counter electrode.The negative electrode was prepared by mixing the active material of activated carbon (AC) with polyvinylidene fluoride (PVDF) binder in a weight ratio of 9:1 which was homogenized and dispersed in N-methylpyrrolidone (NMP) solution. The slurry was then uniformly pasted on a nickel foam current collector and dried at 60° C in an oven for 8 h to make sure complete evaporation of the NMP. The positive electrode was prepared by mixing the active material (VS_2), carbon black (CB) and polyvinylidene fluoride (PVDF) binder which helped to improve the conductivity of material in a weight ratio of 8:1:1 and dispersed in N-methylpyrrolidone (NMP) solution. The slurry was then uniformly pasted on a nickel foam current collector and also dried at 60° C in an oven for 8 h.

The electrochemical test of the asymmetric cell was carried out in a two- electrode cell configuration by means of coin-type cells with thickness of 0.2 mm and diameter of 16 mm, using a glass micro fibre filter paper as the separator in a 6 M KOH aqueous electrolyte solution. The mass loading of VS_2 (positive electrode) was within 2 - 3 mg and that of AC (negative electrode) with 6 - 9 mg.

Results and Discussion

Figure 1 (a) shows the XRD patterns of the VS_2 powder sample. The wavelength used for the XRD analysis was the 1.7890 Å line of a Co-K_α source. All diffraction peaks designated in the figure correspond to to the pure hexagonal phase of VS_2 (JCPDS 36-1139) with lattice constants of a=b =0.322 Å and c=0.576 Å. The XRD data suggest that VS_2 preferentially grows in the (001) low-index crystallographic direction hence would lead to nanosheets formation. Figure 1 (b) represents the XRD patterns of AC powder. The wavelength used for the XRD analysis was Cu-Kα, 1.5405 Å. All the peaks are identified to graphite peaks (COD:96-900-8570) which crystallizes in the hexagonal structure with space group p63mc(186), lattice parameters $a = 2.4560$ Å and $c = 6.6960$ Å [48].
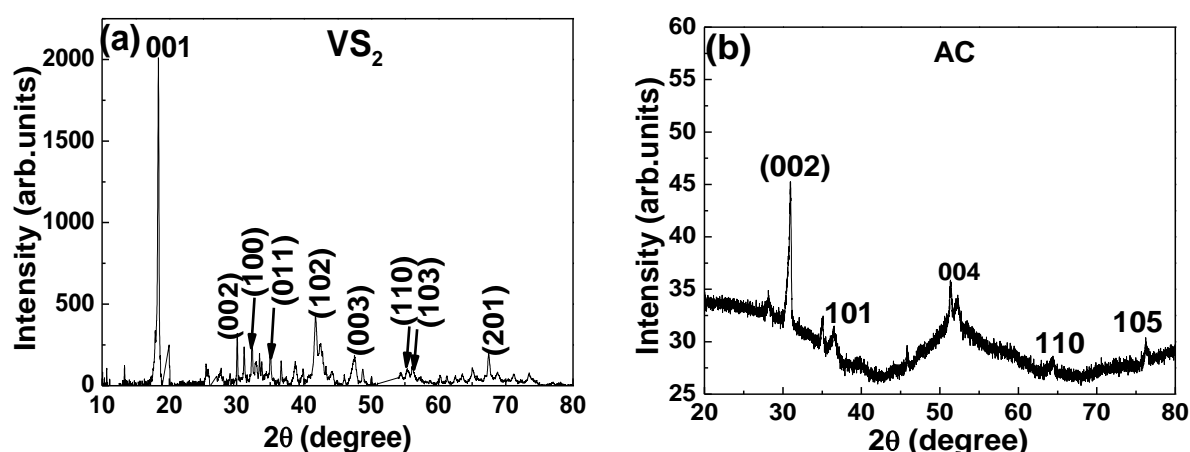
**Figure 1:** X-ray diffraction of (a) VS_2 and (b) AC electrodes.

Figure 2 (a) shows the Raman spectrum of VS_2 electrode. The characteristic peak positions of 278 cm^{-1} and 404 cm^{-1} due to the in-plane E_{2g}^1 and the out-of-plane A_{1g} vibration modes showed the presence of VS_2[49]. The A_{1g} mode was due to the out-of-plane vibration of only the S atoms in opposite directions while the in-plane E_{2g}^1 mode formed from opposite vibration of the two S atoms with respect to the V atom[49].

8

Figure 2 (b) shows two prominent D and G peaks, signifying that the produce AC is fabricated of highly disordered graphitic structures. It shows two distinct peaks at 1344 cm^{-1} (D-band) and 1603 cm^{-1} (G-band). These bands correspond to the disordered carbon/structural defects and graphitic layers (sp^2 bonded carbon atoms) of the carbon material[50] .The intensity ratio of the D-band to that of G-band ($R = I_D/I_G$) is 0.8, and this shows a low degree of graphitic crystalline structure [51].
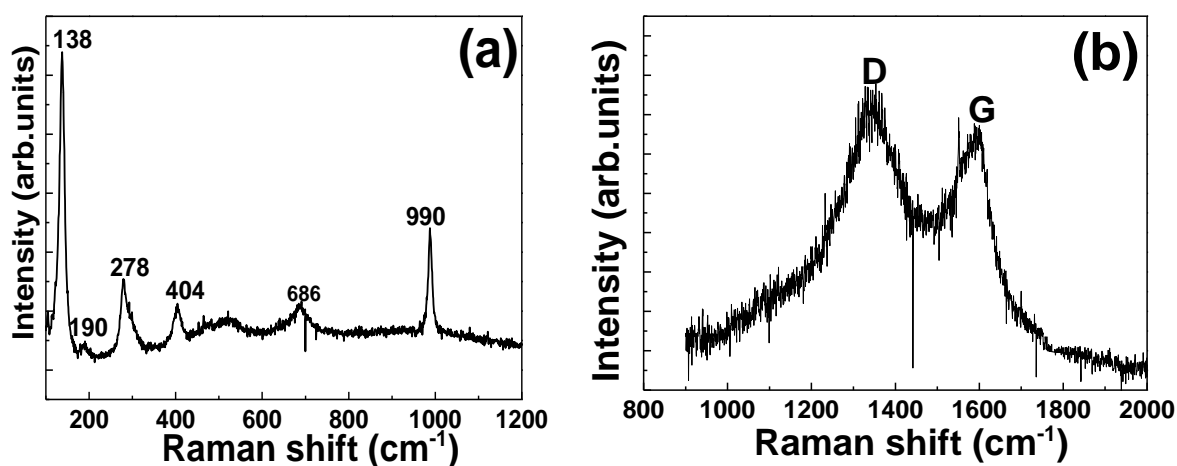

Figure 2: Raman pattern of (a) VS_2 and (b) AC electrodes respectively.

Figure 3 (a) and (b) show the low and high magnification SEM micrographs of the VS_2 sample. It can be seen from the figure that the sample is composed of a large number of nanosheets structure. Figure 3 (c) and (d) present the low and high magnification SEM of the AC sample. As observed in the micrograph, the sample is composed of large interconnected macropores which provide a large ion-accessible surface for fast ion transport in high performance supercapacitors [48].
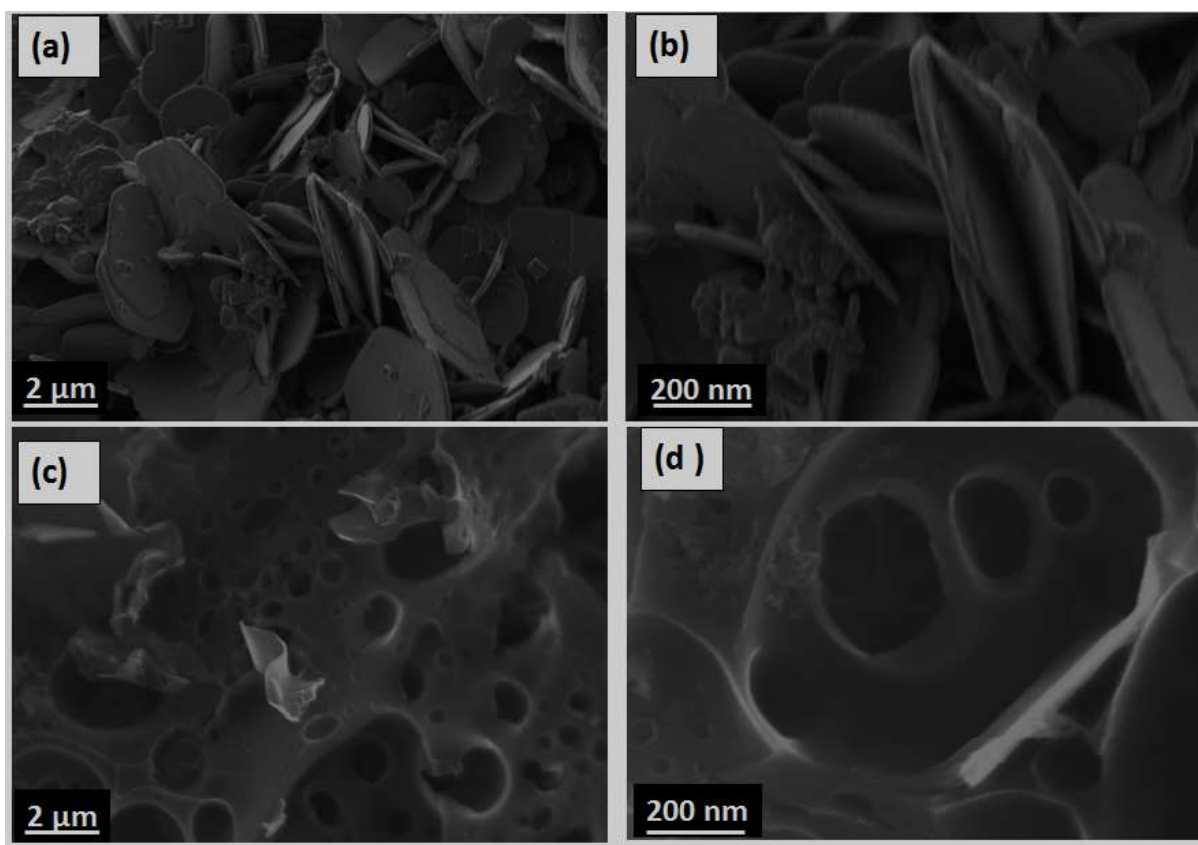
Figure 3: Low and high magnification SEM images of (a) and (b) VS$_2$ (c) and (d) AC electrodes.

The high resolution TEM (HRTEM) image (Figure 4 (a)) of the VS$_2$ nanosheets shows layered VS$_2$ sheets with an interlayer spacing of 0.26 nm (upper inset to the figure) which corresponds to the (001) plane of the hexagonal phase of VS$_2$. The lower inset to Figure 4 (a) shows the selected area electron diffraction (SAED) pattern of a single nanosheets which is well indexed to the single crystalline hexagonal phase of VS$_2$. Figure 4 (c) shows TEM of activated carbon with large particles.
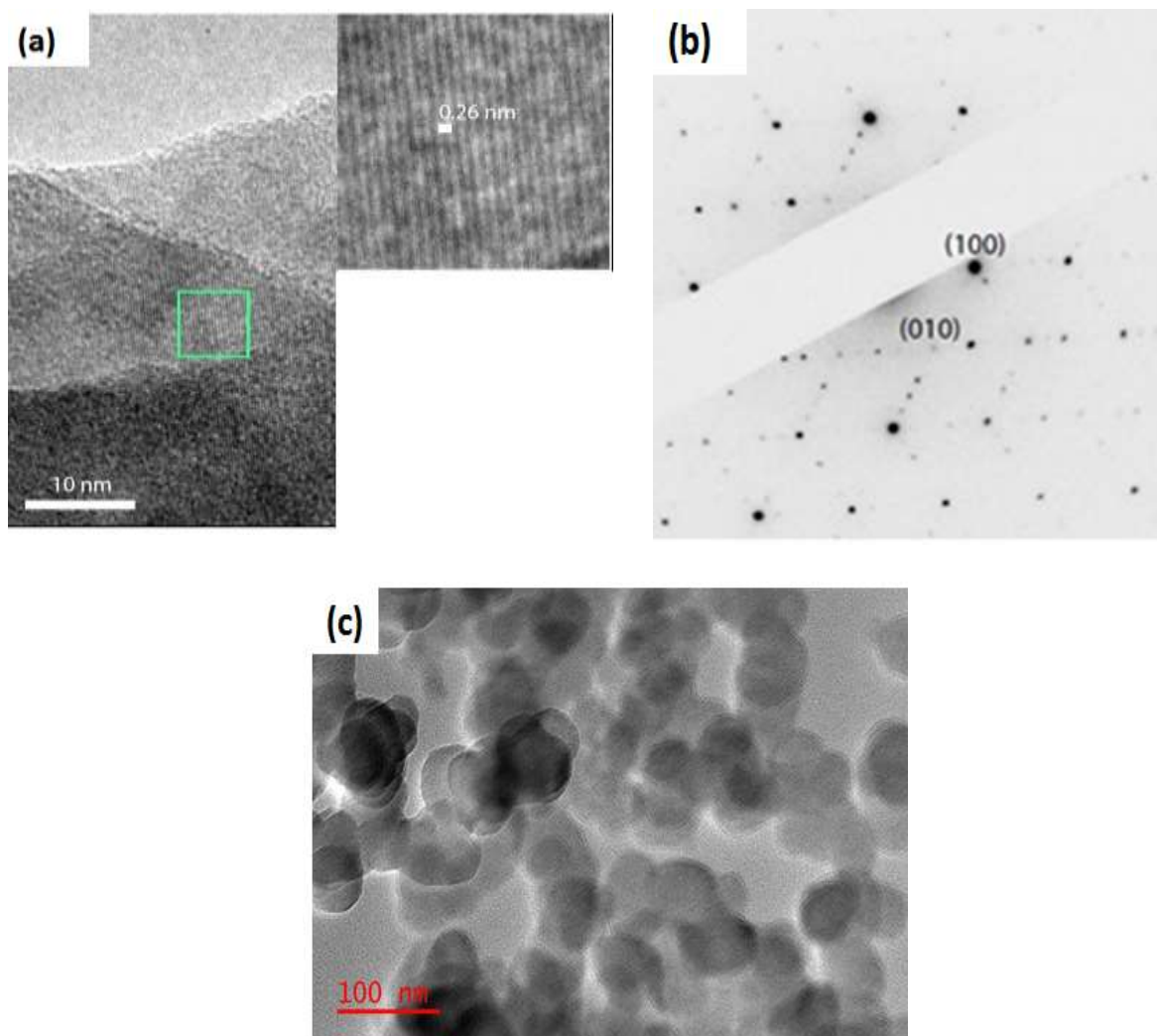
Figure 4: HRTEM images of (a) VS_2 nanosheets with the insets to the figure showing d spacing (upper) (b) SAED pattern VS_2 nanosheets and (c) the AC sample, respectively.

The corresponding EDX pattern in Figure 5 (a) confirms that the synthesized VS_2 composite is composed of elements of Vanadium and Sulfur atoms in the sample.
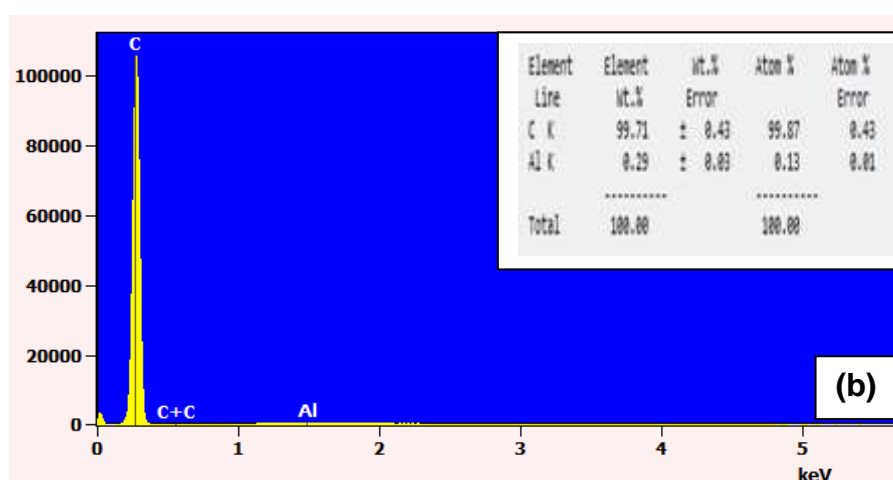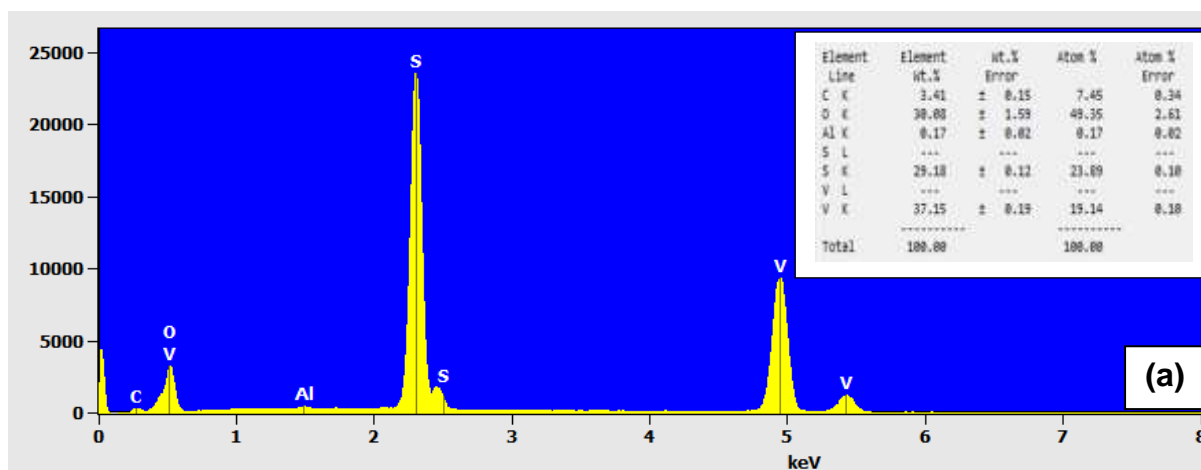
Figure 5: EDX pattern of (a) VS$_2$ and (b) AC electrodes respectively.

Figure 5 (b) confirms that activated carbon is composed of carbon .The elements Al are present due to the signals from the copper grid used as a sample holder for microscopy analysis.

The chemical composition of VS$_2$ was also confirmed by XPS as shown in Figure 6. Before ion sputtering, C, O, V and S elements are detected in the survey, however, after ion sputtering for 30 minutes, only V and S elements are detected and that suggests that the appearance of C and O in the initial survey could be due to surface-adsorbed CO$_2$ and O$_2$ (see Figure 6 (a). Figure 6 (b) and (c) show high resolution scans of V 2p and S 2p respectively. The energy positions of the V- peaks which correspond to 513.5 eV and 521.1 eV (V 2p$_{3/2}$ and V 2p$_{1/2}$) indicate a V valence of +4 [52,53]. The S peaks corresponding to S 2p at energy of

161.4 eV comprises of S $2p_{1/2}$ (160.5 eV) and S $2p_{3/2}$ (161.9 eV) peaks which are orbitals of divalent sulfide ions. Therefore, the survey after ion sputtering (showing only V and S elements) correspond to a pure VS_2 phase.
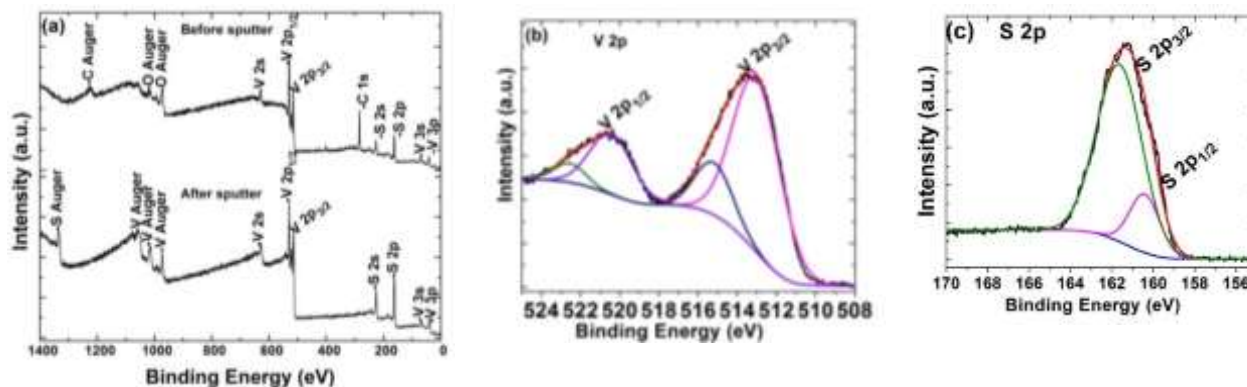
Figure 6: (a) VS_2 XPS survey spectrum, and high resolution scans of (b) V 2p, (c) S 2p

Figure 7 (a) and (b) represent the BET results from the surface area and porosimetry analysis carried out on the VS_2 and the AC samples respectively. The nitrogen adsorption-desorption isotherm of the VS_2 show a type III behaviour with H3 hysteresis isotherm (Figure 4 (a)), indicating a weak interaction between the N_2 adsorbent and the material. On the other hand, the N_2 adsorption-desorption isotherm of the AC presents (Figure 4 (b)) a typical type I adsorption–desorption that characterize complex materials containing micropores. Sample with a corresponding specific surface area (SSA) of 5.5 m^2 g^{-1} and 1040 m^2 g^{-1} for the VS_2 and AC samples respectively. In addition, the nature of the pore structure present in the VS_2 nanosheets are mainly mesoporous with a broad pore size distribution of 2–7 nm (inset to Figure 7 (a)) while a micropores structure is recorded in the AC samples with an average pore size of 2.7 nm (inset to figure 7 (b)).
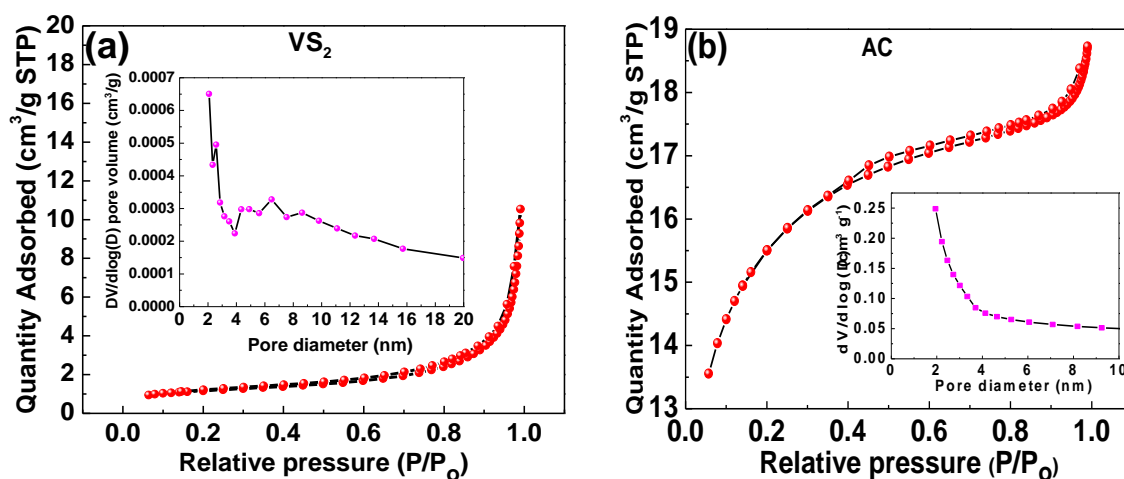
Figure 7: (a) and (b) the N_2 adsorption–desorption isotherm of the VS_2 nanosheets and AC respectively (insets show pore size distribution)

Electrochemical performances of VS_2 nanosheets and activated carbon

To evaluate the potential applications of the electrode materials for supercapacitor applications, the individual electrochemical properties of the VS_2 and AC electrodes were firstly studied in a three-electrode system using 6 M KOH electrolyte. Cyclic voltammetry (CV), chronopotentiometry (CD) and electrochemical impedance spectroscopy (EIS) measurements were carried out for both samples. Figure 8 (a) shows the CV curves of the VS_2 electrode at scan rates of 5, 10, 20, 50 and 100 mV s^{-1}, respectively. A pair of redox peaks corresponding to anodic peak at ~ 0.25 V and cathodic peak ~ 0.34 V is visible in all the CV curves, revealing distinct faradic characteristics. Therefore the anodic peak is due to the oxidation of V^{3+} to V^{4+} whereas the cathodic peak is due to the reverse process. With an increase in the scan rates, the small shift in both cathodic and anodic peak potentials are considered to have a direct relationship with internal resistance of the electrode, respectively, indicating that the fast redox reactions occur at the electroactive material/electrolyte interface. Figure 8 (b) shows the CV curves of AC electrode at various scan rates ranging from 5 to 100 mV s^{-1}. These CV curves show relatively rectangular shapes without redox peaks which are typical electric double-layer capacitive sample behaviour.

Figure 8 (c) shows the galvanostatic charge/discharge curves of VS$_2$ electrode at different current densities within a potential range of 0 - 0.5 V. Each discharge curve includes two clear voltage steps: A fast potential drop from 0.50 V to 0.35 V and a voltage plateau from 0.35 V to 0.22 V. The voltage plateau at around 0.3 V suggests a typical faradic characteristic which is in good agreement with the CV curves reported in Figure 8 (a). Figure 8 (d) shows the galvanostatic charge/discharge curves of AC electrode at different current densities within a potential range of -0.8 - 0 V. As can be seen from Figure 8 (d), the shapes of the charge and discharge curves are very similar to each other and show typical electric double-layer capacitive characterized by a nearly symmetrical triangular shape. This is in agreement with the results from CV curves in Figure 8 (b). Based on the galvanostatic charge–discharge (CD) curves, the specific capacitance of the VS$_2$ and AC electrodes were calculated using the Eq. (1):

$$C_m = \frac{I \times t}{m \times \Delta V} \tag{1}$$

where I is the discharge current (A), t is the discharge time (s), m is the mass of active material (g), ΔV is the potential range of discharge (V), and C_m is the specific capacitance (F/g). The specific capacitances of VS$_2$ and AC electrodes were calculated at different current densities and the plot of the specific capacitance (F g^{-1}) of the VS$_4$ nanosheets and AC electrodes as a function of current density (A g^{-1}) is shown in Figure 8 (e). The good performance of VS$_2$ nanosheets can be attributed to the open structure of the VS$_2$ electrode which can facilitate the penetration of electrolyte ions into the inner part and shorten the ionic diffusion path, therefore improving the dynamic electrochemical performance. The activated carbon revealing that the porous cavities are interconnected in size of several micrometres with a substantial amount of macropores which offer enough reservoirs for electrolyte which is highly required for improved supercapacitor electrode performance[47].
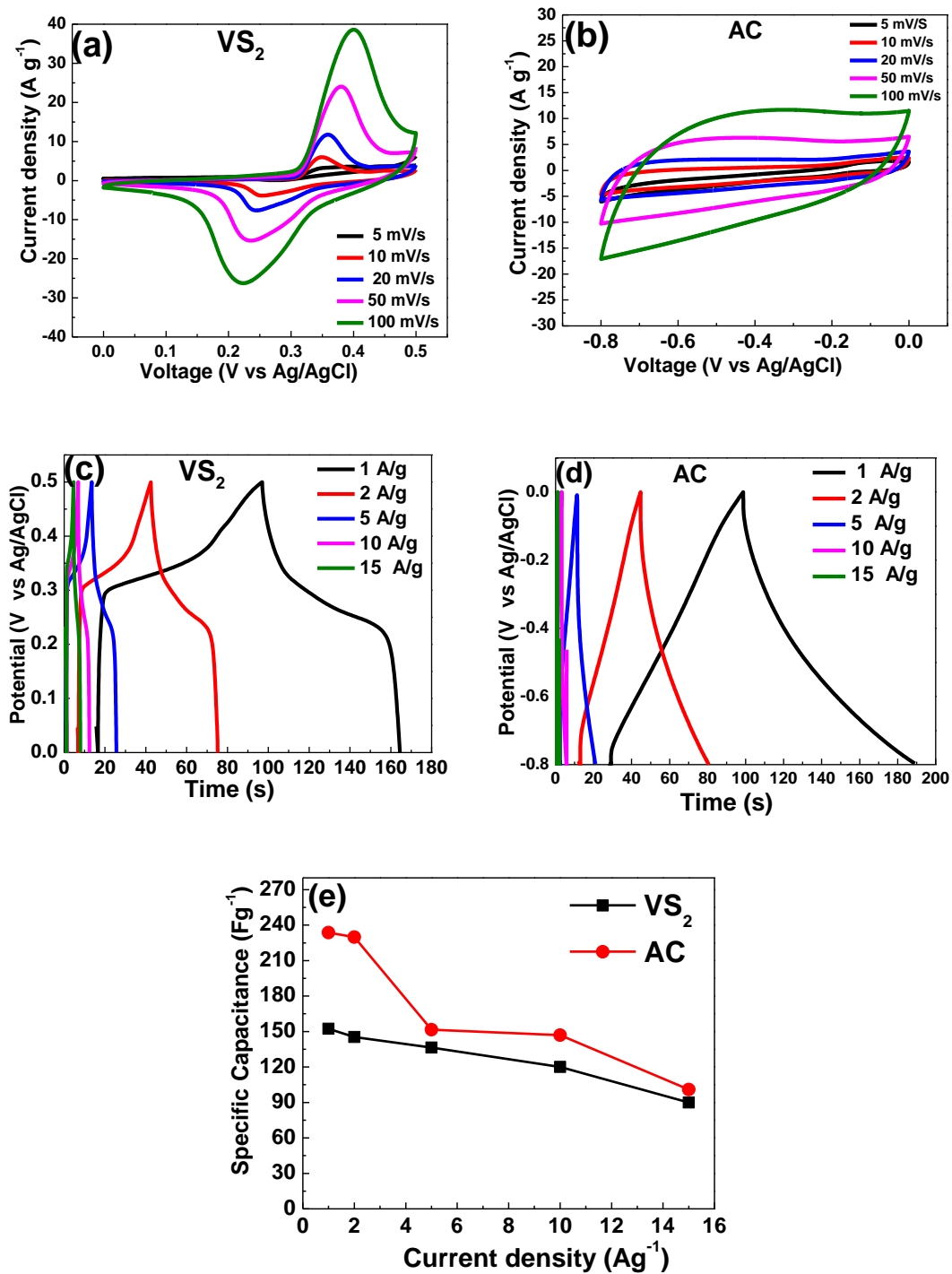
Figure 8: (a) and (b) Cyclic voltammetry at scan rates of 5-100 mV s^{-1}; (c) and (d) Galvanostatic charge–discharge at current densities of 1 - 15 A g^{-1}; (e) specific capacitance versus current densities of the VS$_2$ and AC electrodes respectively.

Electrochemical properties of the asymmetric supercapacitor

To further assess the potential application of the VS_2 nanosheets array electrode in supercapacitors, an asymmetric supercapacitor was fabricated in which the positive electrode comprised of the VS_2 material and the activated carbon material was used as the negative electrode. In order to obtain the optimal performance of the asymmetric full cell supercapacitors, a charge balance $Q_+ = Q_-$ between the two electrodes was done; where Q_+ and Q_- are the charges stored in the positive and negative electrodes, respectively. The charge can be expressed by [54]:

$$Q = C_s \times m \, \Delta U \tag{2}$$

where Cs is the specific capacitance of the active material, m is the mass of each active material and ΔU is the potential range during the charge–discharge process.

In order to get $Q_+ = Q_-$, the mass balancing follows the equation

$$\frac{m_+}{m_-} = \frac{C_{s-} \Delta U_-}{C_{s+} \, \Delta U_+} \tag{3}$$

For making two electrode cells, according to Eqn (3), the mass of the VS_2 electrode should be two times mass of the AC electrode.

From figure 9 (a), it is expected that the operating cell voltage could be extended to about 1.4 V in 6 M KOH solution as electrolyte if the VS_2 electrode as a cathode and the AC electrode as an anode are assembled into asymmetric ECs (figure 9)

Figure 9 (b) shows the CV curves of VS_2//AC asymmetric device measured at different scan rates from 5 to 200 mV s^{-1}. It indicates that the CV curves simultaneously express the faradic and electric double-layer capacitive behaviour which is the typical characteristics of hybrid asymmetric supercapacitors. An asymmetric charge–discharge curve showing the existence of both faradic behaviour from 0.55 - 0.15 V and the electric double-layer 0.55 V - 1.4 V behaviour at all current densities (figure 9 (c)) were observed.
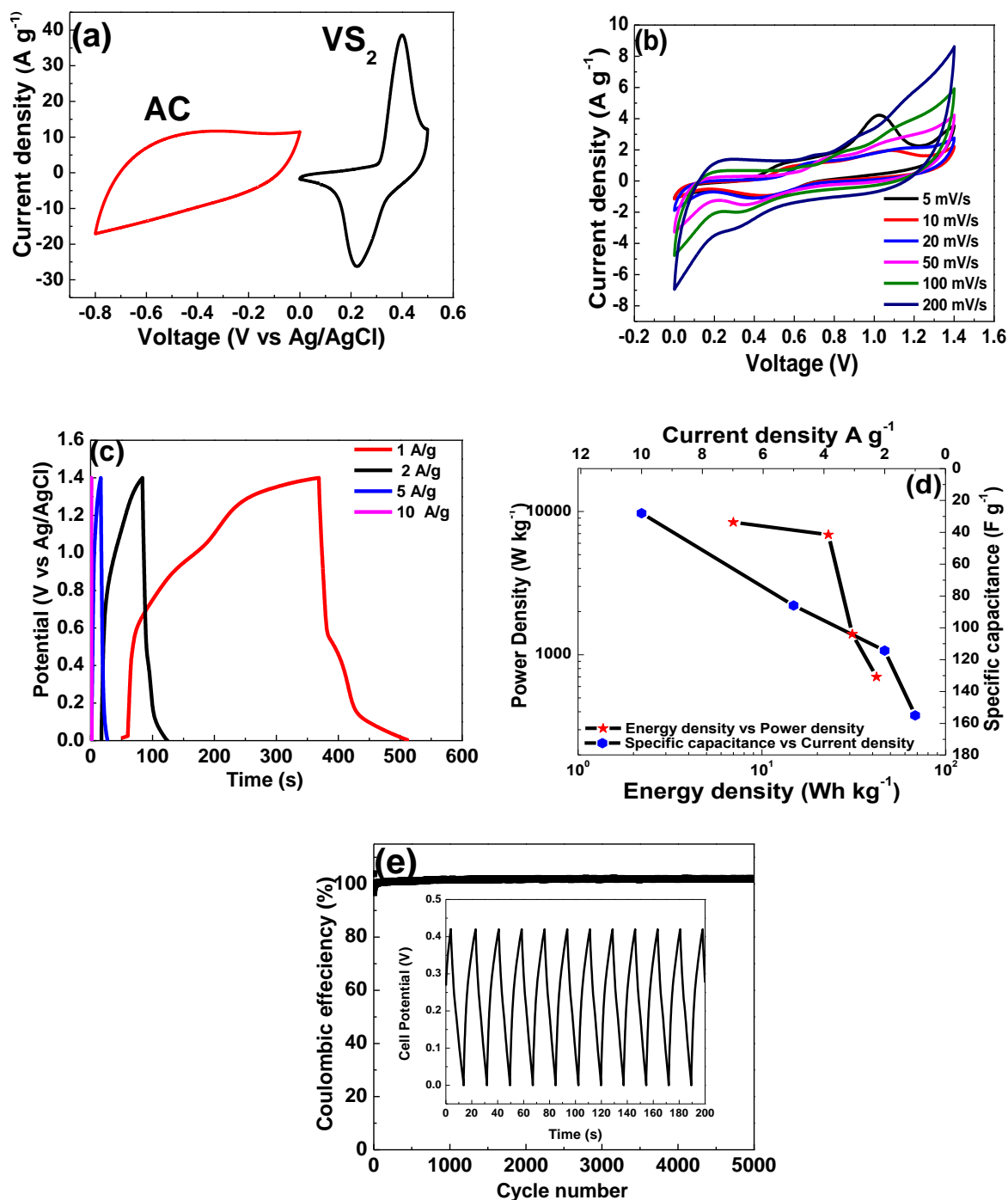
Figure 9: (a) Cyclic voltammetry of VS_2 nanosheets and activated carbon electrodes at scan rates of 50 mV s^{-1} for three-electrode setup; asymmetric VS_2//AC device (b) Cyclic voltammetry at scan rates of 50 – 500 mV s^{-1} (c) Galvanostatic charge–discharge of at current densities of 1 - 15 A g^{-1} and (d) Ragone plot and the specific capacitance as function of the current density and (e)cycle stability at a constant current density of 2 A g^{-1} respectively.

18

The energy density (E, in W h kg^{-1}) and power density (P, in W kg^{-1}) of ECs can be calculated from specific capacitance, C_s according to the following equations:

$$E = \frac{1}{2}C_s\Delta U^2 = \frac{1000 \times C_s \times \Delta U^2}{2 \times 3600} = \frac{C_s \times \Delta U^2}{7.2} \qquad (4)$$

$$p = \frac{E}{t} = \frac{3600 \times E}{1000 \times \Delta t} = \frac{3.6 \times E}{\Delta t} \qquad (5)$$

where U is the voltage window of the full cell and Δt is the discharge time.

The Ragone plot and the specific capacitance as function of the current density of the asymmetric device are shown in figure 9 (d). The specific capacitance of the VS$_2$//AC can reach 155 F g^{-1} at a current density of 1 A g^{-1} calculated from eq (2).

The maximum energy density of the device was recorded as 42 W h kg^{-1} with a corresponding power density of 700 W Kg^{-1} at a current density of 1 A g^{-1} as shown in figure 9 (d). The VS$_2$//AC asymmetric shows a much improved energy density at high power density in comparison with other asymmetric devices involving AC as negative electrode such AC//Ni(OH)$_2$/XC-72 energy density of 36 Wh/kg and corresponding power density of 490 W/kg at 0.5 Ag^{-1})[55], Ni(OH)$_2$@3D Ni-AC energy density of 21.8 Wh kg^{-1} and corresponding power density of 660 Wkg^{-1} at 1 Ag^{-1})[56] and CuS//AC (energy density of 15.06 W h kg^{-1} and corresponding power density of 392.9 W kg^{-1} at 0.5 Ag^{-1}) [57].

The stability of the electrode material is also a very important characteristic for their application as energy storage devices. In order to understand the stability of VS$_2$//AC asymmetric device, the samples were subjected to 5000 cycles at the high current density of 2 A g^{-1} as shown in figure 9 (e). The coulombic efficiency of VS$_2$//AC after 5000 cycles is ~ 99% and exhibit excellent electrochemical stability.
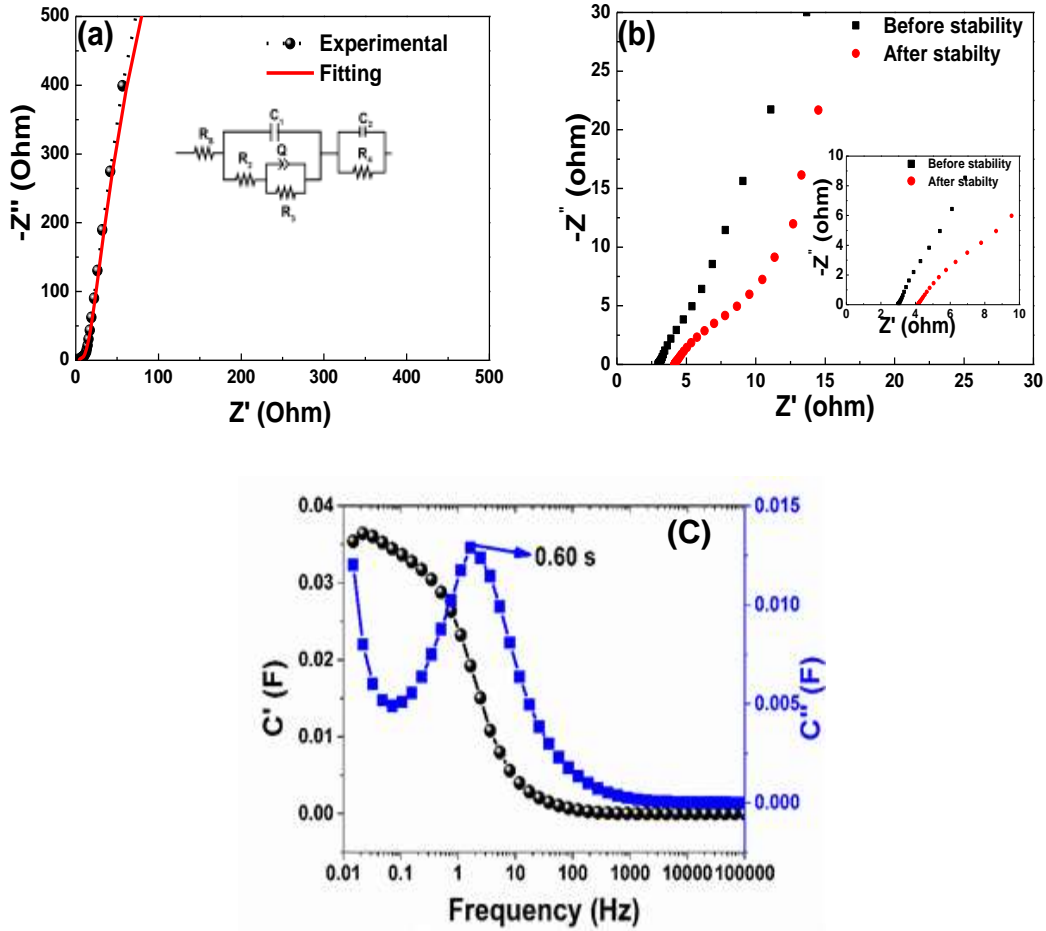
Figure 10: (a) EIS plot and fitting curve for the asymmetric cell, (b) EIS before and after cycling, (c) the real and the imaginary part of the cells capacitance against frequency of asymmetric cell of VS$_2$//AC respectively

Figure 10 (a) presents the Nyquist plot of the asymmetric device with an R$_s$ value of 2.97 Ω obtained from the fitted plot using the circuit shown in the inset to the Figure. The Nyquist plot before and after cycling is shown in figure 10 (b). From this, an R$_s$-intercept value of 2.97 Ω before cycling and 4.10 Ω after cycling was obtained.

The frequency response of porous carbon electrodes has been modelled with a single series resistor-capacitor (RC) circuit [58]. Based on this model, the real and imaginary part of the capacitance as a function of the frequency can be calculated using equations below;

$$C = \frac{-1}{(\omega Z")} \tag{6}$$

$$C(\omega) = C'(\omega) - jC^{"}(\omega) \tag{7}$$

$$C' = \frac{Z^{"}(\omega)}{\omega \, |Z(\omega)|^2} \tag{8}$$

$$C^{"} = \frac{Z'(\omega)}{\omega \, |Z(\omega)|^2} \tag{9}$$

where Z is the complex impedance written as $Z(\omega) = Z'(\omega) + Z^{"}(\omega), \omega = 2\pi f,$. $C'(\omega)$ represents the real accessible capacitance of the cell at the corresponding frequency which signifies the deliverable capacitance, while $C^{"}(\omega)$ represents the energy loss due to the irreversible process of the electrodes Z' and $Z^{"}$ represents the real and imaginary parts of the Nyquist plot respectively [58]. Based on the above formulae, the capacitance (C') of the cell is 0.035 F (from topmost part of the C' graph) as shown in figure 10 (b), C'' define the transition frequency between a pure resistive behaviour and pure capacitive of the asymmetric with a relaxation time of 0.6 s achieved by taking the reciprocal of the maximum frequency in the C'' graph figure 10 (c). This value display that the cell can be fully charged within a very short time.

Conclusions

We have successfully fabricated an asymmetric supercapacitor cell based on porous activated carbon material as negative electrodes and VS_2 as positive electrode. The asymmetrical device displays high specific capacitance of 155 F g^{-1} at 1 A g^{-1} with a maximum energy density of 42 Wh kg^{-1} and power density of 700 W kg^{-1}. In addition, the recorded great stability with $\sim$ 99% capacitance retention and no capacitance loss after 5000 cycles at a current density of 2 Ag^{-1} at an operating voltage of about 1.4 V in 6 M KOH aqueous electrolytes showing that pairing such hybrid materials could be an excellent method to produce supercapacitors with high energy and power densities. These results offer a convenient and effective way to fabricate asymmetric hybrid supercapacitors based on VS_2

and AC with high energy density while maintaining the high power density property of supercapacitor.

ACKNOWLEDGEMENTS

References

1   A. S. Arico, P. Bruce, B. Scrosati, J.-M. Tarascon and W. van Schalkwijk, *Nat Mater*, 2005, **4**, 366–377.

2   B. E. Conway, *Conway, B. E. Electrochemical Supercapacitors: Scientific Fundamentals and Technological Applications;*, Kluwer Academic/ Plenum, New York, 1999.

3   W. Van Schalkwijk and B. Scrosati, *Advances in lithium-ion batteries*, Springer Science & Business Media, 2002.

4   L. Zhang, F. Zhang, X. Yang, G. Long, Y. Wu, T. Zhang, K. Leng, Y. Huang, Y. Ma, A. Yu and Y. Chen, *Sci. Rep.*, 2013, **3**, 1408.

5   L. L. Zhang and X. S. Zhao, *Chem. Soc. Rev.*, 2009, **38**, 2520–2531.

6   J. W. Long, B. Dunn, D. R. Rolison and H. S. White, *Chem. Rev.*, 2004, **104**, 4463–4492.

7   Y.-G. Wang, L. Cheng and Y.-Y. Xia, *J. Power Sources*, 2006, **153**, 191–196.

8   S.-B. Ma, K.-W. Nam, W.-S. Yoon, X.-Q. Yang, K.-Y. Ahn, K.-H. Oh and K.-B. Kim, *Electrochem. commun.*, 2007, **9**, 2807–2811.

9   V. Ganesh, S. Pitchumani and V. Lakshminarayanan, *J. Power Sources*, 2006, **158**, 1523–1532.

10   H. Inoue, T. Morimoto and S. Nohara, *Electrochem. Solid-State Lett.*, 2007, **10**, A261–A263.

11   T.-W. Lin, C.-S. Dai, T.-T. Tasi, S.-W. Chou, J.-Y. Lin and H.-H. Shen, *Chem. Eng. J.*, 2015, **279**, 241–249.

12   W. Lin, W. Yu, Z. Hu, W. Ouyang, X. Shao, R. Li and D. S. Yuan, *Electrochim. Acta*, 2014, **143**, 331–339.

13   T. Peng, H. Wang, H. Yi, Y. Jing, P. Sun and X. Wang, *Electrochim. Acta*, 2015, **176**, 77–85.

14   J.-W. Lang, L.-B. Kong, M. Liu, Y.-C. Luo and L. Kang, *J. Solid State Electrochem.*, 2010, **14**, 1533–1539.

15   Q. T. Qu, Y. Shi, L. L. Li, W. L. Guo, Y. P. Wu, H. P. Zhang, S. Y. Guan and R. Holze, *Electrochem. commun.*, 2009, **11**, 1325–1328.

16   D. Xuan, W. Chengyang, C. Mingming, J. Yang and W. Jin, *J. Phys. Chem. C*, 2009, **113**, 2643–2646.

17   B. G. Choi, S.-J. Chang, H.-W. Kang, C. P. Park, H. J. Kim, W. H. Hong, S. Lee and Y. S. Huh, *Nanoscale*, 2012, **4**, 4983–4988.

18   P. Tang, L. Han and L. Zhang, *ACS Appl. Mater. Interfaces*, 2014, **6**, 10506–10515.

19   P. Simon and Y. Gogotsi, *Acc. Chem. Res.*, 2012, **46**, 1094–1103.

20   Y.-G. Wang, Z.-D. Wang and Y.-Y. Xia, *Electrochim. Acta*, 2005, **50**, 5641–5646.

21   M. Kumar, A. Subramania and K. Balakrishnan, *Electrochim. Acta*, 2014, **149**, 152–158.

22   S. J. Zhu, J. Zhang, J. J. Ma, Y. X. Zhang and K. X. Yao, *J. Power Sources*, 2015, **278**, 555–561.

23   Y. Xiao, Y. Cao, Y. Gong, A. Zhang, J. Zhao, S. Fang, D. Jia and F. Li, *J. Power Sources*, 2014, **246**, 926–933.

24   H. R. Ghenaatian, M. F. Mousavi and M. S. Rahmanifar, *Electrochim. Acta*, 2012, **78**, 212–222.

25   Y. Zhou, N. Lachman, M. Ghaffari, H. Xu, D. Bhattacharya, P. Fattahi, M. R. Abidian, S. Wu, K. K. Gleason, B. L. Wardle and others, *J. Mater. Chem. A*, 2014, **2**, 9964–9969.

26   M.-Y. Cho, S.-M. Park, J.-W. Lee and K.-C. Roh, *J. Electrochem. Sci. Technol.*, 2011, **2**, 152–156.

27   Y. Wang, L. Yu and Y. Xia, *J. Electrochem. Soc.*, 2006, **153**, A743–A748.

28   T. Brousse, P.-L. Taberna, O. Crosnier, R. Dugas, P. Guillemet, Y. Scudeller, F. Favier, Y. Zhou, P. Simon and D. Blanger, in *Meeting Abstracts*, 2006, p. 125.

29   L.-M. Chen, Q.-Y. Lai, Y.-J. Hao, Y. Zhao and X.-Y. Ji, *J. Alloys Compd.*, 2009, **467**, 465–471.

30   S. W. Lee, J. Kim, S. Chen, P. T. Hammond and Y. Shao-Horn, *ACS Nano*, 2010, **4**, 3889–3896.

31   M. A. Bissett, I. A. Kinloch and R. A. W. Dryfe, *ACS Appl. Mater. Interfaces*, 2015, **7**, 17388–17398.

32   S. Nohara, T. Asahina, H. Wada, N. Furukawa, H. Inoue, N. Sugoh, H. Iwasaki and C. Iwakura, *J. Power Sources*, 2006, **157**, 605–609.

33   D. P. Dubal, G. S. Gund, C. D. Lokhande and R. Holze, *Energy Technol.*, 2014, **2**, 401–408.

34   W. Tang, L. Liu, S. Tian, L. Li, Y. Yue, Y. Wu and K. Zhu, *Chem. Commun.*, 2011, **47**, 10058–10060.

35   S. Surendran, K. V. Sankar, L. J. Berchmans and R. K. Selvan, *Mater. Sci. Semicond. Process.*, 2015, **33**, 16–23.

36   K. Krishnamoorthy, G. K. Veerasubramani, S. Radhakrishnan and S. J. Kim, *Mater. Res. Bull.*, 2014, **50**, 499–502.

37   J. Feng, X. Sun, C. Wu, L. Peng, C. Lin, S. Hu, J. Yang and Y. Xie, *J. Am. Chem. Soc.*, 2011, **133**, 17832–17838.

38   P. Justin and G. R. Rao, *Int. J. Hydrogen Energy*, 2010, **35**, 9709–9715.

39   S. Ratha, S. R. Marri, N. A. Lanzillo, S. Moshkalev, S. K. Nayak, J. N. Behera and C. S. Rout, *J. Mater. Chem. A*, 2015, **3**, 18874–18881.

40   L. Li, S. Kim, W. Wang, M. Vijayakumar, Z. Nie, B. Chen, J. Zhang, G. Xia, J. Hu, G. Graff and others, *Adv. Energy Mater.*, 2011, **1**, 394–400.

41   H. A. Therese, F. Rocker, A. Reiber, J. Li, M. Stepputat, G. Glasser, U. Kolb and W. Tremel, *Angew. Chemie Int. Ed.*, 2005, **44**, 262–265.

42   J. Feng, L. Peng, C. Wu, X. Sun, S. Hu, C. Lin, J. Dai, J. Yang and Y. Xie, *Adv. Mater.*, 2012, **24**, 1969–1974.

43   P. Mohan, J. Yang, A. Jena and H. Suk Shin, *J. Solid State Chem.*, 2015, **224**, 82–87.

44   F. Cao, W. Hu, L. Zhou, W. Shi, S. Song, Y. Lei, S. Wang and H. Zhang, *Dalt. Trans.*, 2009, 9246–9252.

45   C. Song, K. Yu, H. Yin, H. Fu, Z. Zhang, N. Zhang and Z. Zhu, *J. Mater. Chem. C*, 2014, **2**, 4196–4202.

46   C. S. Rout, R. Khare, R. V. Kashid, D. S. Joag, M. a. More, N. a. Lanzillo, M. Washington, S. K. Nayak and D. J. Late, *Eur. J. Inorg. Chem.*, 2014, **2014**, 5331–5336.

47   A. Bello, F. Barzegar, D. Momodu, J. Dangbegnon, F. Taghizadeh and N. Manyala, *Electrochim. Acta*, 2015, **151**, 386–392.

48   F. Barzegar, A. Bello, D. Y. Momodu, J. K. Dangbegnon, F. Taghizadeh, M. J. Madito, T. M. Masikhwa and N. Manyala, *RSC Adv.*, 2015, **5**, 37462–37468.

49   X. Liu, H.-L. Shuai and K.-J. Huang, *Anal. Methods*, 2015, **7**, 8277–8284.

50   G. Ma, D. Guo, K. Sun, H. Peng, Q. Yang, X. Zhou, X. Zhao and Z. Lei, *RSC Adv.*, 2015, **5**, 64704–64710.

51   W. Gao, L. B. Alemany, L. Ci and P. M. Ajayan, *Nat. Chem.*, 2009, **1**, 403–408.

52   J. Mendialdua, R. Casanova and Y. Barbaux, *J. Electron Spectros. Relat. Phenomena*, 1995, **71**, 249–261.

53   T.-H. Yang, S. Nori, H. Zhou and J. Narayan, *Appl. Phys. Lett.*, 2009, **95**, 2506.

54   A. Bello, F. Barzegar, D. Momodu, J. Dangbegnon, F. Taghizadeh, M. Fabiane and N. Manyala, *J. Power Sources*, 2015, **273**, 305–311.

55   L. Sui, S. Tang, Z. Dai, Z. Zhu, H. Huangfu, X. Qin, Y. Deng and G. M. Haarberg, *New J. Chem.*, 2015, **39**, 9363–9371.

56   Y.-Z. Su, K. Xiao, N. Li, Z.-Q. Liu and S.-Z. Qiao, *J. Mater. Chem. A*, 2014, **2**, 13845–13853.

57   J. Zhang, H. Feng, J. Yang, Q. Qin, H. Fan, C. Wei and W. Zheng, *ACS Appl. Mater. Interfaces*, 2015, **7**, 21735–21744.

58   P. L. Taberna, P. Simon and J.-F. Fauvarque, *J. Electrochem. Soc.*, 2003, **150**, A292–A300.